GSA Data Repository 2015286

Modes and rates of horizontal deformation from rotated river basins: Application to the Dead Sea fault system in Lebanon

Liran Goren[1], Sébastien Castelltort[2], and Yann Klinger[3]

[1]Geological and Environmental Sciences, Ben-Gurion University of the Negev, Beer Sheva, 84105, Israel.

[2]Section des Sciences de la Terre et de l'Environnement, Université de Genève, Rue des Maraîchers 13, 1205 Geneva, Switzerland

[3]Institut de Physique du Globe de Paris, Sorbonne Paris Cité, Université Paris Diderot, UMR7154 CNRS, 75238 Paris, France

RIVER ORIENTATION AND DEVIATION

We evaluate the orientation of nine basins that drain Mount Lebanon to the west and span the full mountain flank from the coast to the main water divide. The orientation is defined by using a weighted orthogonal linear regression through the pixels of each of the nine basins. The weight is a function of the upstream drainage area, such that pixels with greater area are assigned a larger weight (Fig. DR1). Table DR1 shows the measured azimuth of the nine basins using the weighted orthogonal linear regression.
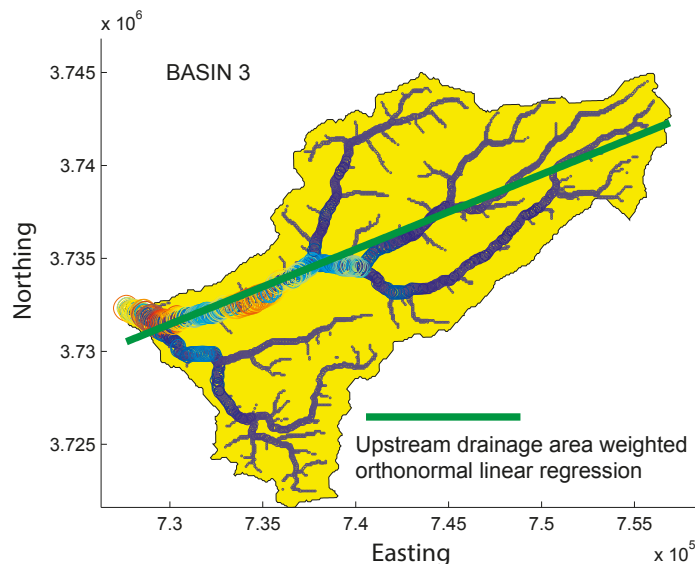

Figure DR1: Example of a weighted orthogonal linear regression for basin 3 (see Fig. 1 in the main text and Fig. DR5 for location). All basin pixels are accounted for by the regression. To show the fluvial network, pixels that drain less than 50 pixels are colored in yellow.

Next, we estimate the deviation of the rivers from a strike-perpendicular orientation. The reason is that drainage of linear mountain ranges, such as Mount Lebanon, has been shown to flow transverse to the strike of the orogen (Hovius, 1996). Since the crest of Mount Lebanon is parallel to the Yammouneh Fault (YF), which has an azimuth of 30° (northeast), perpendicular drainage towards the Mediterranean should be at 300°. Table DR1 shows the calculated deviation.

TABLE DR1: RIVER AZIMUTH AND DEVIATION.

	Azimuth	Deviation (θ)
1[1]	227.31[2]	72.7
2	255.24	44.8
3	259.55	40.5
4	262.18	37.8
5	257.86	42.1
6	262.36	37.6
7a	290.7	9.6
7b	298.77	1.2
8	279.56	20.4

[1] Basin numbering from south to north. See Fig.1 in the main text and Fig. DR 5 for basins location.
[2] Only for the segment to the east of the Roum Fault

RIVER DISEQUILIBRIUM FROM χ ANALYSIS

The definition of χ following equation (1) is:

$$\chi(x) = \int_0^x \left(\frac{A_0}{A(x')}\right)^{\frac{m}{n}} dx', \qquad \text{(S1)}$$

where A is the upstream drainage area, A_0 is an arbitrary scaling area, x is a coordinate system along the channel path, and m and n are positive empirical constants. The ratio, m/n, is commonly referred to as the concavity index. The calculation of χ is based on extraction of flow path and accumulation of drainage area from a 90m SRTM digital elevation model (Jarvis, 2008), and applying a drainage area cutoff of 1 km^2 to define the fluvial network. Construction of the χ map requires choosing the arbitrary drainage area, A_0, which we set to 1 m^2, and a value for the concavity index, m/n. The concavity index is determined by an iterative process (Perron and Royden, 2013; Goren et al., 2014b; Willett et al., 2014): χ values for the network are generated with different m/n values. Then, we examine the behavior of the rivers in a plot of elevation versus χ (χ-z plot). The reason is that under stable geometry and topology of the drainage network, the slope of a river in a χ-z plot is defined as $(U/KA_0^m)^{1/n}$, where U is the rock uplift rate and K is the erosivity (Perron and Royden,

2013; Royden and Perron, 2013). For too high or too low concavity index the channels exhibit large scattering with highly variable slopes in the χ-z plot as if each tributary experienced different pattern and history of U or K (Yang et al. 2015). Supplementary figure DR2 shows χ-z plots for various values of m/n that range between 0.1-0.6. When choosing a value for m/n, we search for χ-z profiles with small scatter within each basin separately. We do not formally look for the most linear profiles (which implies constant U and K in time and scape) and we do not formally minimize the overall scatter in the χ-z plot, because part of the scatter represents the disequilibrium state of the landscape (Willett et al., 2014). We find that for a concavity index of 0.3, the χ-z plot exhibits relatively small scattering within each basin separately. Figure DR3 shows χ mapping with different values of m/n. It is clear from the figure that although the choice of m/n changes the value of χ, it does not affect its spatial pattern. We use m/n=0.3 in the remaining of the analysis.
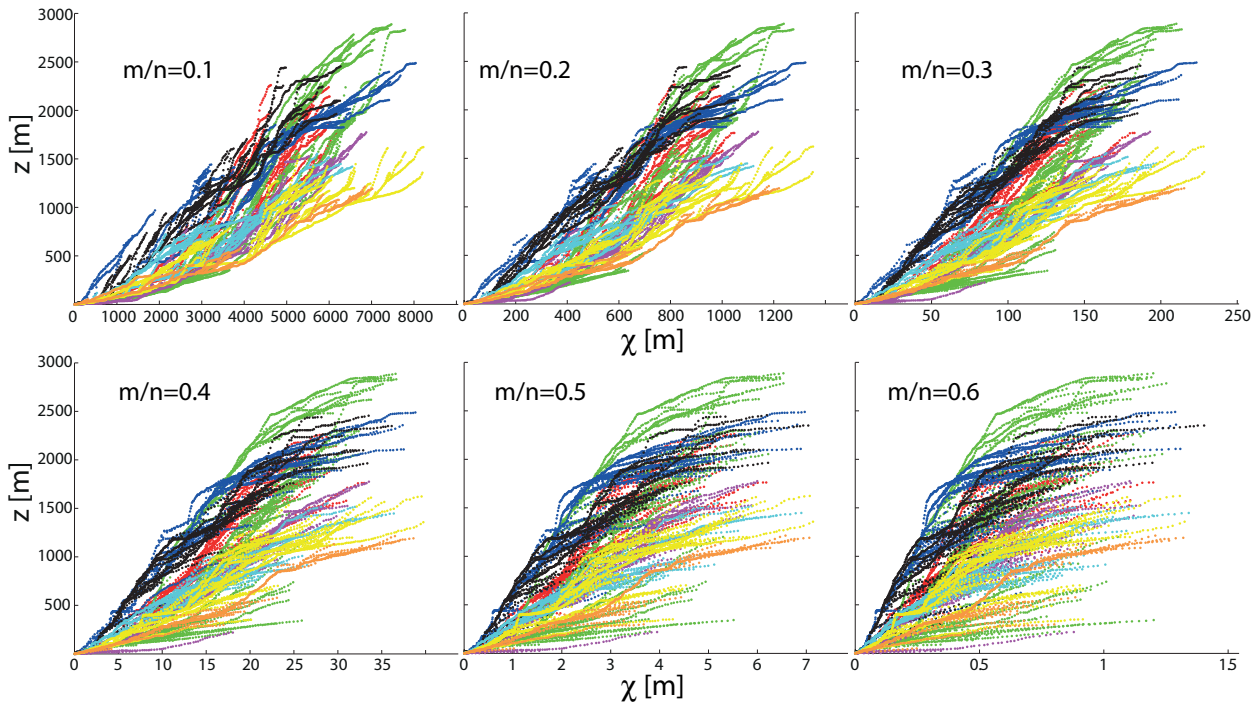

Figure DR2: χ-z plots for the eight basins that drain Mount Lebanon to the west. Each basin is assigned with a color (See Fig. DR4 for color scheme). For m/n = 0.3 the internal scatter within each basins is relatively small.

The effect of spatial non-uniformity in U and K on the value of χ is estimated by calculating the average slope, $dz/d\chi$, of each basin separately and evaluating it as $(U/KA_0^m)^{1/n}$. Figure DR4 shows a pattern of increasing χ-z slope from the north to the center of the mountain range that then decreases further south. This pattern might reflect a spatial variability of the tectonic rock uplift rate, U, or the erosivity, K, such that $(U/KA_0^m)^{1/n}$ is highest in between the two highest peaks of Qurnat as Sawda' and Mount Sannine. Note that the pattern of periodic χ differences across divide

emerges despite the decrease in $(U/KA_0^m)^{1/n}$ towards the south. With this decrease, and under steady-state assumption, the χ of the northern tributaries of each basin is expected to be smaller with respect to the southern tributaries, while the opposite is observed. Furthermore, figure DR5 shows that the interpretation that the χ pattern represents disequilibrium drainage area and transient divides is consistent with landscape morphology of asymmetric hillslope with steeper slopes towards low-χ tributaries, and perched high χ tributaries relative to their lower χ neighbors.
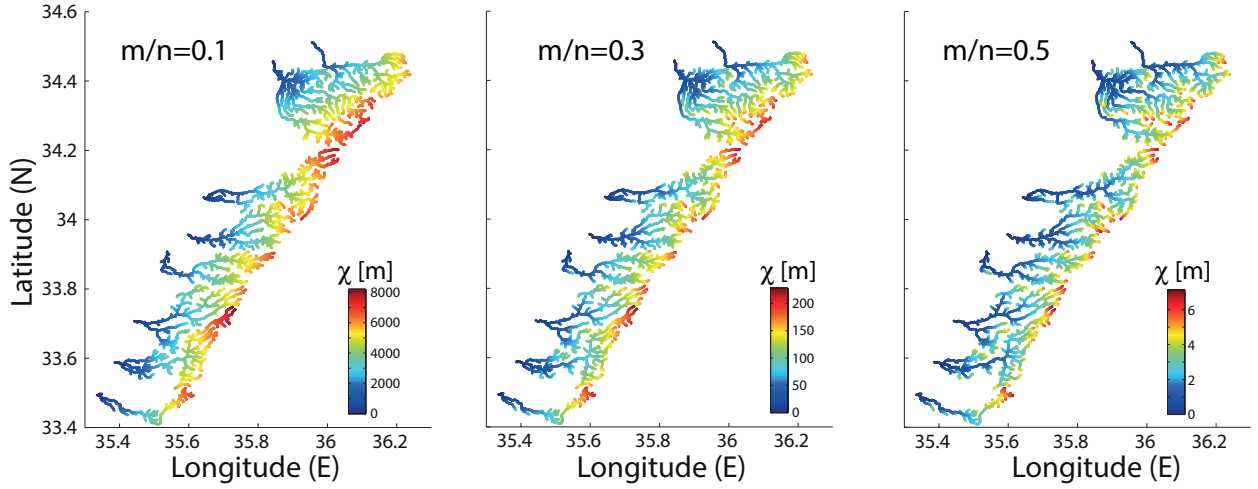

Figure DR3: χ maps of western Mount Lebanon rivers using different values of concavity index, m/n. Although the absolute value of χ changes, the pattern of χ differences across inter-basin divides remain the same.
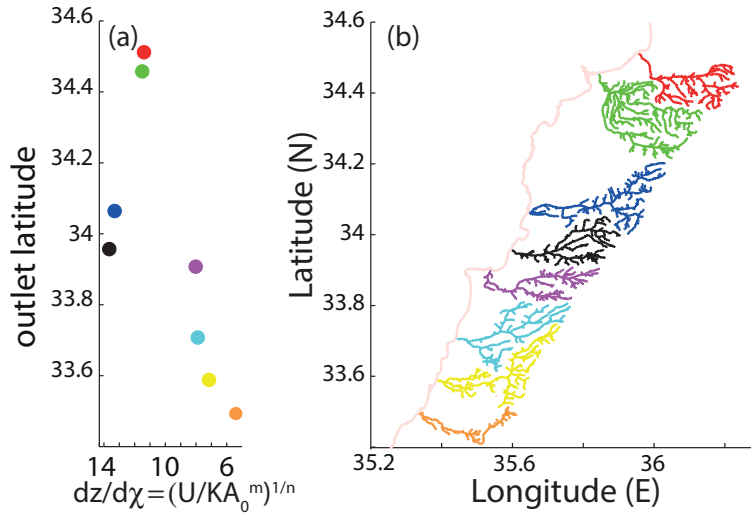

Figure DR4: (a) Average slope of the χ-z curves from figure DR2 with m/n=0.3. (b) The eight basins that are considered in the analysis. The color code here is the same as in figure DR2.
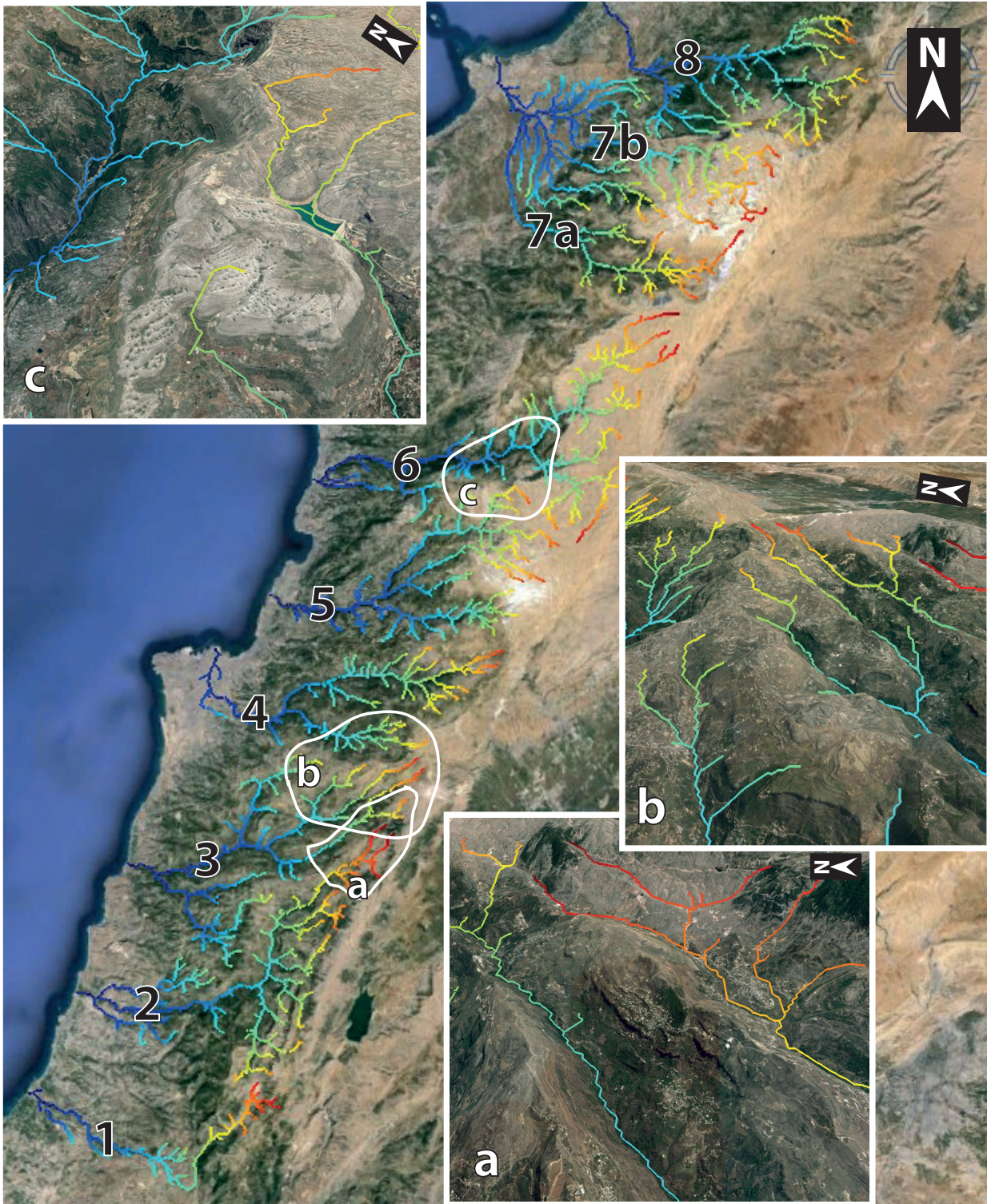
Figure DR5: Google Earth images of western Mount Lebanon with superimposed χ values along main channels. Insets a, b, and c show that high-χ tributaries tends to be perched above neighboring low-χ tributaries as predicted by theory. kml χ-map file is supplied as part of the supplementary information.

KINEMATIC MODEL

To study the deformation imposed by the velocity field of equations (2) and (3) in the main text on western Lebanon rivers, we consider a single line-river. During progressive deformation, the headwater of the line-river, point '*h*' (intersection of the river and the YF) (Fig. 2 in the main text), migrates southward at velocity V_f, and its position is defined by $y_h(t)=t.V_f$, where t is time since the onset of deformation, and $y_h(0)=0$. The westernmost point of the line-river, '*o*', is at distance R_c from the YF, where R_c is the width of the zone along which the distributed deformation affects the river pattern, and is smaller or equal to R_d, the width of the band of deformation. During the deformation, point o migrates southward (faster than the headwater) and eastward. $x_o(t)$ and $y_o(t)$ are the x and y coordinates of point o at time t, such that $x_o(0)=R_c$ and $y_o(0)=0$. $l(t) = y_o(t)- y_h(t)$ is the y-axis projection of the river segment that we consider (Fig. 2 in the main text).

We use the fault perpendicular velocity field, U, from equation (2) in the main text, to express the time derivative of $x_o(t)$:

$$\frac{dx_o(t)}{dt} = U[x_o(t)] = -\frac{U_p}{R_d}x_o(t), \qquad (S2)$$

where U_p is the far field plate velocity in the direction perpendicular to the fault. The solution of equation (S2) with the initial condition $x_o(0)=R_c$ is:

$$x_o(t) = R_c\exp\left(-\frac{U_p}{R_d}t\right). \qquad (S3)$$

Similarly, we can express the time derivative of $l(t)$, the projection of the river on the y-axis at time t using the fault parallel velocity field, V, from equation (3) in the main text:

$$\frac{dl(t)}{dt} = V[x_o(t)] - V_f = \frac{V_p-V_f}{R_d}x_o(t) = \frac{V_p-V_f}{R_d}R_c\exp\left(-\frac{U_p}{R_d}t\right), \qquad (S4)$$

where V_p is the parallel component of the far-field plate velocity. The solution of equation (S4) with the initial condition $l(0)=0$ is:

$$l(t) = \frac{V_p-V_f}{U_p}R_c\left[1\text{-}\exp\left(-\frac{U_p}{R_d}t\right)\right]. \qquad (S5)$$

Finally we note that the orientation of the river, $\theta(t)$, can be evaluated as:

$$\tan\theta(V_f) = \frac{l(t)}{x_o(t)}. \qquad (S6)$$

By using equations (S3) and (S5), $\theta(t)$ becomes:

$$\tan\theta(V_f) = \frac{l(t)}{x_0(t)} = \frac{V_p-V_f}{U_p}\left[\exp\left(\frac{U_p}{R_d}t\right) - 1\right]. \qquad (S7)$$

Equation (S7) describes the orientation of the river as a function of time. We add to this description another parameter, $R_h=y_h(t)= t.V_f$, such that R_h is the distance of the headwater of basin 6 from the origin (the fault kink) at time t. We use the definition of R_h to eliminate t from equation (S7):

$$\tan\theta(V_f) = \frac{V_p - V_f}{U_p}\left[\exp\left(\frac{U_p}{R_d}\frac{R_h}{V_f}\right) - 1\right]. \qquad (S8)$$

Equation (S8) describes the orientation of the rivers, θ, as a function of the slip rate along the YF, V_f (Fig. 3 in the main text), and appears as equation (4) in the main text.

KINEMATIC MODEL WITH SIMPLE SHEAR ONLY

Here, we find the amount of rotation for a scenario where deformation is a function of the fault parallel velocity, V, alone. This is relevant for measurements of paleomagnetic rotation about a vertical axis, which are insensitive to the pure shear component (expressed by the gradient in the perpendicular velocity, U). The calculation is based on the assumption that $x_o(t)=R_c$ for all t. In this case:

$$\frac{dl(t)}{dt} = V[x_0(t)] - V_f = \frac{V_p - V_f}{R_d}x_0(t) = \frac{V_p - V_f}{R_d}R_c \qquad (S9)$$

and

$$l(t) = \frac{V_p - V_f}{R_d}R_c t . \qquad (S10)$$

$\theta(t)$ is then evaluated as:

$$\tan\theta\left(V_f\right) = \frac{l(t)}{x_0(t)} = \frac{V_p - V_f}{R_d}\frac{R_h}{V_f}. \qquad (S11)$$

Figure DR6 shows the deviation of the rivers, θ, as a function of the slip rate along the YF, V_f, based on equation (S11).
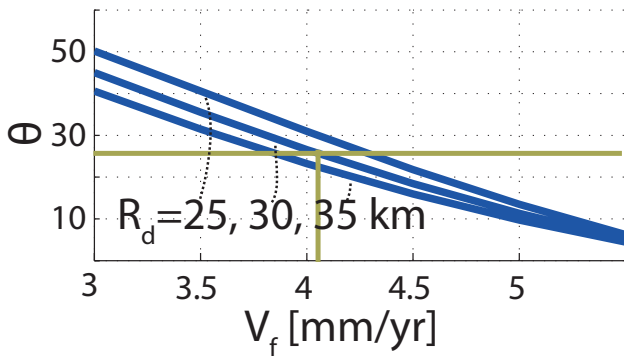

Figure DR6: Relations between slip rate on the YF, V_f, and rotation of a line-marker, θ, in a model of simple shear only, showing that for V_f=4.1 mm/yr, the rotation is ~25°.

THE ARABIA-SINAI FAR FIELD RELATIVE PLATE VELOCITY

In the application of our kinematic model, V_p and U_p are the components of the relative plate velocity between the west and the east sides of the YF. To evaluate them, we use the Arabia - Sinai - Africa plate kinematic model of Le Pichon and Gaulier (1988) that is based on McKenzie (1970),

Izzeldin (1982) and Garfunkel (1981). Le Pichon and Gaulier (1988) decompose the relative motion of Sinai, Africa and Arabia into three periods for which the poles of rotation are computed: pre-13 Ma when there is no relative motion between Arabia and Sinai, 13-4.7 Ma when there is relative motion between Sinai and both Arabia and Africa, and 4.7-0 Ma when there is no relative motion between Sinai and Africa. We use these poles of rotation as input to the Unavco plate motion calculator (http://www.unavco.org) and compute the relative velocity between Arabia and Sinai along a line parallel to the YF and tangent to the Tripoli-Beirut thrust system.

The calculation is performed at eight points (labeled A-H, Fig. DR7) spaced 20 km from each other parallel to the YF. During the last period of 4.7 Myr the scatter in the velocity magnitude between the eight sites is only 6.4% and the scatter in the azimuth is only of 6°. During the period of 13–4.7 Ma the scatter in the velocity magnitude is only of 4.6% and the scatter in the azimuth is only of 4°. We therefore decompose the velocity vectors into two components, parallel and perpendicular to the YF, and we calculate the averages of these components for each of the periods separately (see Table DR2). Finally, we take a weighted average of the two periods. The weights are found by an iterative process were we resolve the duration of the distributed deformation recorded by the rivers, and we update the weights of the two periods accordingly. The final weights are based on our inference that the distributed deformation resolved by the rivers lasted ~ 7.35 Myr. The weight assigned to the older period is 2.65 Myr/7.35 Myr and the weight assigned to the younger period is 4.7 Myr/7.35 Myr. The results are that the average far field Arabia-Sinai relative plate velocity since 7.35 Ma are V_p=7.0 mm/yr parallel to the YF and U_p=4.2 mm/yr perpendicular to the YF. These are the values that we use in the analysis.
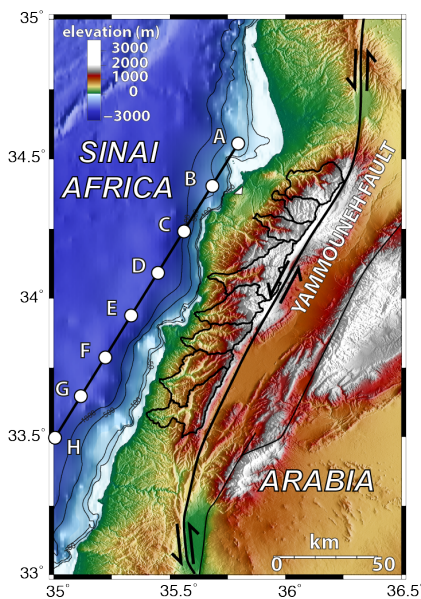

Figure DR7: Stations where the far field relative Sinai-Arabia plate velocity is calculated from the poles of rotations of Le Pichon and Gaulier (1988)

Table DR2: FAR FIELD ARABIA-SINAI RELATIVE PLATE VELOCITY
BASED ON LE PICHON AND GAULIER (1988).

Plates / Period / Pole	Site	Latitude °N	Longitude °E	Velocity magnitude (mm/yr)	Azimuth (cw from N)	Fault parallel (mm/yr)	Fault perpendicular (mm/yr)
Arabia –	A	34.550655	35.788469	8.6	355.3	7.1	4.9
Sinai+Africa	B	34.396882	35.675957	8.5	356.8	7.1	4.7
/	C	34.239251	35.560657	8.4	356.7	7.0	4.6
4.7-0 Ma	D	34.086240	35.450984	8.4	357.4	7.0	4.5
/	E	33.928581	35.339066	8.3	358.1	7.0	4.4
32.75 °N	F	33.776385	35.229414	8.2	358.9	7.0	4.2
22.64 °E	G	33.623384	35.118110	8.1	359.6	7.0	4.1
	H	33.460008	35.004165	8.1	0.4	7.0	4.0
Average				**8.3**		**7.0**	**4.4**
	A	34.550655	35.788469	8.0	358.3	6.8	4.2
Arabia – Sinai	B	34.396882	35.675957	7.9	358.8	6.8	4.1
/	C	34.239251	35.560657	7.9	359.3	6.8	4.0
13-4.7 Ma	D	34.086240	35.450984	7.8	359.8	6.8	3.9
/	E	33.928581	35.339066	7.8	0.3	6.7	3.8
32.53 °N	F	33.776385	35.229414	7.7	0.8	6.7	3.8
17.45 °E	G	33.623384	35.118110	7.7	1.3	6.7	3.7
	H	33.460008	35.004165	7.6	1.9	6.7	3.6
Average				**7.8**		**6.8**	**3.9**

LANDSCAPE EVOLUTION MODELING WITH DAC

We perform a numerical simulation of a Mount Lebanon like domain by using the landscape evolution model DAC, Divide And Capture, (Goren et al., 2014a). DAC solves for the evolution of fluvial topography through a combination of numerical and analytical solutions on different scales. The evolution of large-scale fluvial channels is solved numerically on a dynamic, relatively sparse, and irregular grid. Numerical grid points are uplifted according to an imposed tectonic rock uplift rate history, and advected horizontally following a horizontal velocity field. Fluvial vertical incision is modeled by an implicit solver of the detachment-limited stream power model (Howard, 1994). The analytical component solves explicitly for the location of water divides in between any two adjacent channels (Goren et al., 2014a).

In the simulation, the domain size is 200x60 km (note that figure 4 of the main text and the 2015286-Movie.mov show only portions of the domain). To maintain a constant volume domain, material is constantly being incorporated into the mountain range across the northern boundary and western base level (Castelltort et al., 2012). Material leaves the domain through the southern boundary. The tectonic rock uplift rate is constant in time, but it varies in space along strike. At the

center of the domain it is set to 0.4 mm/yr, and it tapers down linearly to a value of 0.3 mm/yr at the north end of the domain and to 0.1 mm/yr at the south end of the domain. The erosivity, $K=kP^m$, is a function of the precipitation, P, and the erodibility, k. In the numerical domain we simulate an 800 m of relatively hard rock with $k = 2 \times 10^{-5}$ $m^{0.1}/yr^{0.7}$ below which lies a layer of softer rock with $k = 3 \times 10^{-5}$ $m^{0.1}/yr^{0.7}$. During the simulation, the harder rock layer erodes away, and in some places softer rocks are exposed. Simulation results show preservation of relic landscapes with hard rocks at the high elevations. In addition, hard rocks dominate the western base level as these rocks are being advected into the mountain. Overall, the lithological pattern in the western side is consistent with the geological map of Lebanon (Daëron, 2005). The values of U, P, and k where chosen to represent the pattern of $(U/KA_0^m)^{1/n}$ that is observed in figure DR4. Note that parameters and model results do not represent the landscape along the eastern side of Mt. Lebanon.

TABLE DR3: DAC SIMULATION PARAMETERS

Parameter	Value	Comments
U, tectonic rock uplift rate	0.1-0.4 mm/yr	
P, precipitation rate	800 mm/yr	
k, erodibility	2-3×10⁻⁵ m⁰·¹/yr⁰·⁷	The erosivity, K, is defined as $K = kP^m$
x_c, Hillslope length	700 m	
θ_c, critical hillslope angle	26°	
Hillslope diffution coefficient	0.2 m²/yr	
m, Drainage area exponent	0.3	
n, Slope exponent	1	
h, Hack's law exponent	2	Used for distance to area conversion in the analytical component of DAC: $A = k_a x^h$
k_a, Hack's law coefficient	2/3	Used for distance to area conversion in the analytical component of DAC: $A = k_a x^h$
V_p, far field to the south	6.0 mm/yr	
V_f, strike-slip on the fault	4.1 mm/yr	
U_p, far field to the east	4.2 mm/yr	
U_f, dip-slip on the fault	0 mm/yr	

SUPPLEMENTARY MOVIE DR1: Simulation using DAC landscape evolution model with parameters from table DR3 and a discontinuity in the velocity field, representing the YF, 32 km to the east of the western base level. Simulated time is 7.35 Myr. Left: Evolution of lithology, color coded by the erodibility. Center: Evolution of the drainage network, color coded by χ values. Right: Evolution of topography, color coded by elevation. Note that the geomorphic and tectonic

parameters were chosen to represent the western flank of Mt. Lebanon and hence the eastern side of the model does not represent the eastern flank of Mt. Lebanon.

2015286-GoogleEarth.kml file: The kml file can be opened and viewed with Google Earth. The file shows the χ pattern of western Lebanon rivers. χ values are calculated with $A_0 = 1$ km^2 and m/n = 0.3.

SUPPLEMENTARY REFERENCES

Castelltort, S., Goren, L., Willett, S.D., Champagnac, J.D., Herman, F., and Braun, J., 2012, River drainage patterns in the New Zealand Alps primarily controlled by plate tectonic strain: Nature Geoscience, doi:10.1038/NGEO1582.

Daëron, 2005, Role, cinématique et comportement sismique a long terme de la faille de Yammouneh, principale branche décrochante du coude transpressif libanais (faille du Levant), PhD Thesis, IPGP.

Garfunkel, Z., 1981, Internal structure of the Dead Sea leaky transform (rift) in relation to plate kinematics. Tectonophysics, v. 80, p. 81-108.

Goren, L., Willett, S.D., Herman, F., and Braun, J., 2014a, Coupled numerical–analytical approach to landscape evolution modeling: Earth Surface Processes and Landforms, v. 39, no. 4, p. 522–545, doi:10.1002/esp.3514.

Goren, L., Fox, M., and Willett, S.D., 2014b, Tectonics from fluvial topography using formal linear inversion: Theory and applications to the Inyo Mountains, California: Journal of Geophysical Research - Solid Earth, doi:10.1002/2014JF003079.

Hovius, N., 1996, Regular spacing of drainage outlets from linear mountain belts: Basin Research, v. 8, no. 1, p. 29–44, doi:10.1111/j.1365-2117.1996.tb00113.x

Howard, A.D., 1994, A Detachment Limited Model of Drainage-Basin Evolution: Water Resources Research, v. 30, no. 7, p. 2261–2285, doi:10.1029/94WR00757.

Izzeldin, A.Y., 1982, On the structure and evolution of the Red Sea based on geophysical data from the central and northern part. PhD Thesis, Strasbourg Univ.

Jarvis, A., Reuter, H.I., Nelson, A., and Guevara, E., 2008, Hole-filled seamless SRTM data V4, International Centre for Tropical Agriculture (CIAT), available from http://srtm.csi.cgiar.org.

Le Pichon, X., and Gaulier, J., 1988, The rotation of Arabia and the Levant fault system: Tectonophysics, v. 153, no. 1-4, p. 271–294, doi:10.1016/0040-1951(88)90020-0.

McKenzie, D.P., Davies, D., and Molnar, P., 1970, Plate tectonics of the Red Sea and East Africa. Nature, v. 26, p. 243-248.

Perron, J.T., and Royden, L., 2013, An integral approach to bedrock river profile analysis: Earth Surface Processes and Landforms, doi:10.1002/esp.3302.

Royden, L., and Perron, J. T., 2013, Solutions of the stream power equation and application to the evolution of river longitudinal profiles, J. Geophys. Res. Earth Surf., 118, 497-518, doi:10.1002/jgrf.20031.

Willett, S.D., McCoy, S.W., Perron, J.T., Goren, L., and Chen, C.Y., 2014, Dynamic Reorganization of River Basins: Science, v. 343, no. 6175, doi:10.1126/science.1248765.

Yang, R., Willett, S.D., and Goren, L., 2015, In situ low-relief landscape formation as a result of river network disruption: Nature, v. 520, no. 7548, p. 526–529, doi:10.1038/nature14354